CMS Physics Analysis Summary

Contact: cms-pag-conveners-higgs@cern.ch 2024/10/23

Search for a new heavy scalar boson decaying into a Higgs boson and a new scalar particle in the four b-quarks final state using proton-proton collisions at $\sqrt{s} = 13$ TeV

The CMS Collaboration

Abstract

A search for a massive scalar resonance, X, decaying into a Higgs boson and a scalar, Y, in proton-proton collisions at a centre-of-mass energy of 13 TeV is presented. The search is performed using a data sample corresponding to an integrated luminosity of 138 fb^{-1} collected by the CMS detector. The four b-quark final state is used to probe the possible phenomenon beyond the standard model, $\text{X} \rightarrow \text{YH}$, in which both the Y and the Higgs boson are reconstructed from a pair of b quarks. A range of masses from 400 GeV to 1.6 TeV for the resonance X and from 60 GeV to 1.4 TeV for the scalar Y are investigated. The observations are in agreement with the background-only hypothesis. The largest excess, with a local (global) significance of 4.1 (2.8) standard deviations, is observed for hypothetical X and Y masses of 700 GeV and 400 GeV, respectively. The 95% confidence level limits of the production cross section times branching ratio are presented for all signal mass hypotheses in the range of the search. Results are interpreted within the NMSSM scenario.

1 Introduction

The discovery of the Higgs boson (H) by the ATLAS and CMS Collaborations [1–3] was the experimental confirmation of a cornerstone of the standard model (SM) of particle physics. Many proposed theoretical models of physics beyond the SM (BSM) extend the SM scalar sector with additional fields, resulting in a rich phenomenology with additional scalar particles. Examples of such models are the next-to-minimal supersymmetric SM (NMSSM) [4, 5], the two-real-scalar-singlet extension of the SM [6], and models with warped extra dimensions [7].

The analysis described here explores one possible phenomenology of these theories: the production of a BSM resonance that decays into a SM Higgs boson and a BSM scalar. This is motivated in, for example, NMSSM [8] where a scalar H_{MSSM} or pseudoscalar A_{MSSM} can decay into a SM Higgs boson and a scalar $H_{singlet}$ or pseudoscalar $A_{singlet}$, respectively. The branching ratio for this process $B(H_{MSSM}/A_{MSSM} \to H + H_{singlet}/A_{singlet})$ can be as high as 50% [9–13]. Previous searches for this process have been published by the ATLAS Collaboration, using the $bb\gamma\gamma$ final state [14], and the CMS Collaboration, using the $bb\gamma\gamma$ [15], $bb\tau\tau$ [16], four-b boosted topology [17] final states, and a combination of these three channels [18].

The decay $X \to HH$ is of particular interest, since it can be the manifestation of Randall-Sundrum radion and massive KK graviton production in warped extra dimensions [19, 20], as well as the CP-even scalar predicted by NMSSM [21]. Multiple searches for Higgs boson pair production have been published by the ATLAS and CMS Collaborations in the bbbb [22–24], $bb\tau\tau$ [25, 26], $bb\gamma\gamma$ [27], $bb\ell\nu\ell\nu$ [26, 28], and $bbZZ$ [29] channels, in multiple lepton final states [30], and in combinations of multiple channels [18, 31, 32].

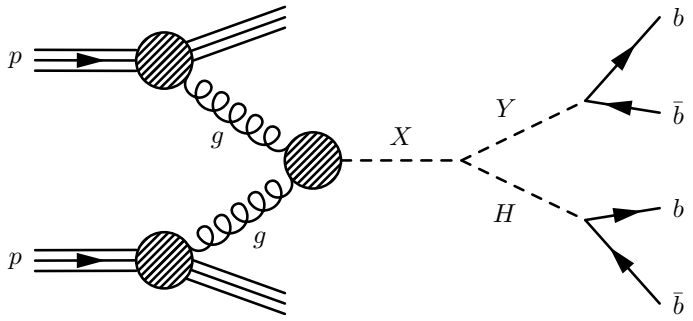

Figure 1: Depiction of the process under investigation, $X \to YH \to b\bar{b}b\bar{b}$.

In order to be sensitive to a broad range of models, a model independent approach is followed in this analysis. Figure 1 depicts an example of X production, in which a heavy scalar resonance X is produced via gluon fusion and then decays into an H and another scalar, Y, with both of them decaying into a $b\bar{b}$ pair.

This work presents a search for X resonances with masses from 400 GeV up to 1.6 TeV and a scalar Y with masses between 60 GeV and 1.4 TeV. The signal is extracted from a two-dimensional fit using the reconstructed masses of the X and Y scalars, m_{Xreco} and m_{Yreco}, respectively. The data samples used for the search correspond to a total integrated luminosity of $138\,fb^{-1}$ collected by the CMS detector in the years 2016, 2017 and 2018. A data-driven approach, utilizing a BDT for reweighting kinematic variables, is implemented for estimating the background. A simultaneous fit to the data samples collected from each year is used when presenting the results in Section 8.

2 The CMS detector

The CMS apparatus [33, 34] is a multipurpose, nearly hermetic detector, designed to trigger on [35, 36] and identify: electrons, muons, photons, and (charged and neutral) hadrons [37–39]. A global "particle-flow" (PF) algorithm [40] aims to reconstruct all individual particles in an event, combining information provided by the all-silicon inner tracker and by the crystal electromagnetic calorimeter (ECAL) and brass-scintillator hadron calorimeter (HCAL), operating inside a 3.8 T superconducting solenoid, with data from the gas-ionization muon detectors embedded in the flux-return yoke outside the solenoid. The reconstructed particles are used to identify τ leptons, jets, and missing transverse momentum [41–43].

The HCAL cells have widths of 0.087 in pseudorapidity (η) and 0.087 in azimuthal angle (ϕ), in the region $|\eta| < 1.74$. In the η-ϕ plane, and for $|\eta| < 1.48$, the HCAL cells map on to 5×5 arrays of ECAL crystals to form calorimeter towers that project radially outwards from a location close to the nominal interaction point. For $|\eta| > 1.74$, the transverse dimensions of these towers increase progressively, up to a maximum of 0.174 in both $\Delta\eta$ and $\Delta\phi$. Within each tower, the energy deposits in ECAL and HCAL cells are summed to define the calorimeter tower energies, which are subsequently used to provide the energies and directions of hadronic jets.

Events of interest are selected using a two-tiered trigger system. The first level (L1), composed of custom hardware processors, uses information from the calorimeters and muon detectors to select events at a rate of around 100 kHz, within a fixed latency of 4 μs [35]. The second level, known as the high-level trigger (HLT), consists of a farm of processors running a version of the full event reconstruction software optimized for fast processing, and reduces the event rate to around 1 kHz before data storage [36].

3 Event reconstruction

The global event reconstruction (also called particle-flow event reconstruction [40]) aims to reconstruct and identify each individual particle in an event, with an optimized combination of all subdetector information. In this process, the identification of the particle type (photon, electron, muon, charged hadron, neutral hadron) plays an important role in the determination of the particle direction and energy.

For each event, hadronic jets are clustered from particle-flow reconstructed particles using the infrared and collinear safe anti-k_{T} algorithm [44, 45] with a distance parameter of 0.4. Jet momentum is determined as the vectorial sum of all particle momenta in the jet, and is found from simulation to be, on average, within 5 to 10% of the true momentum over the whole p_{T} spectrum and detector acceptance. The pseudorapidities of the jets in the events are required to be $|\eta| < 2.4$ for data-taking year 2016 and $|\eta| < 2.5$ for 2017 and 2018.

Additional proton-proton interactions within the same or nearby bunch crossings (pileup) can contribute additional tracks and calorimetric energy depositions to the jet momentum. To mitigate this effect, charged particles identified to be originating from pileup vertices are discarded and an offset correction is applied to correct for remaining contributions. Jet energy corrections are derived from simulation to bring the measured response of jets to that of particle level jets on average. Additional selection criteria are applied to each jet to remove jets potentially dominated by anomalous contributions from various subdetector components or reconstruction failures.

In order to suppress the background originating from leptonic top quark decays, events are ve-

toed if they contain an isolated electron (muon) candidate with $p_T > 15$ (10) GeV and $|\eta| < 2.4$. Criteria for identifying these objects include passing a multivariate identification discriminant and passing selections on isolation and impact parameter with respect to the primary interaction vertex observables.

Jets originating from a b quark (b jets) are identified using the DEEPJET algorithm [46] and the medium b-tagging working point [47]. The working points are defined by the rate of jets that are initiated from up, down, or strange quarks or gluons, but are incorrectly identified as b quark jets. The loose working point is defined by a misidentification rate of 10% and the medium working point is defined by a misidentification rate of 1%. The loose working point has a b-tagging efficiency ranging between 85 - 90% and the medium working point has a b-tagging efficiency ranging between 68% and 78%, depending on the data-taking year.

4 Simulated samples

Signal samples have been generated using MADGRAPH5_aMC@NLO [48] 2.4.2 (2.6.0) for 2016 (2017 and 2018). No particular model is used for signal generation and the only constraint is that the width of the X and Y scalar resonances are each set to 1 MeV, which is negligible compared to the experimental resolution. The parton distribution function (PDF) set NNPDF3.0 with next-to-leading order (NLO) accuracy [49] is used to generate the signal.

Background samples are generated to qualitatively assess the processes that contribute to the background composition and to optimize the event selection. However, this analysis uses a data-driven approach to model the background, described in Section 6, for performing the search for signal in the pp collision dataset. QCD multijet samples, with up to four partons at leading order precision, are generated with MADGRAPH5_aMC@NLO. The production of pairs of top quarks is simulated at NLO precision with POWHEG [50, 51], and events are normalised to the next-to-NLO (NNLO) precision theoretical cross section [52]. Events with a Z boson pair decaying into hadrons, with up to one additional jet emitted at the matrix element level, are simulated with MADGRAPH5_aMC@NLO at NLO precision and normalised to the cross section at NLO precision [53].

For all simulated samples, the parton shower and hadronization is performed with PYTHIA version 8.226 (2016) and PYTHIA version 8.230 (2017 - 2018) [54], and GEANT4 [55] is used for modeling of the CMS detector response.

Contributions due to pileup interactions are simulated and added to the signal and background samples. The simulated events, including both the signal and background samples, are weighted to match the number of pileup interactions observed in data.

5 Event selection and categorization

Events passing a combination of L1 triggers that require the presence of one or more jets are of interest to this analysis. The number of L1 trigger algorithms used for each year is of order 10 and the exact L1 triggers implemented may be different for individual CMS data-taking periods. A range of jet p_T and H_T (the scalar sum of the transverse momentum of all jets in the event) thresholds are used for these triggers. L1 triggers requiring at least one jet in the event can have a p_T threshold on a jet as low as 170 GeV and as high as 200 GeV. L1 triggers only implementing H_T thresholds use values for the threshold as low as 280 GeV and as high as 500 GeV. L1 triggers requiring four jets have H_T thresholds ranging from 250 to 340 GeV with individual p_T selection for each jet; the minimum p_T selection can be as low as 35 GeV for the

lowest p_T jet. Other L1 trigger algorithms are utilized for this analysis, including those with requirements for at least two or at least three jets.

Dedicated HLT algorithms targeting the signal process have been used with selection criteria listed in Table 1. Additionally, each HLT algorithm requires the presence of at least 3 b-tagged jets. The CSV algorithm [47] (2016-2017) and the DEEPCSV algorithm [46] (2018) are used for b tagging at the HLT level. The HLT thresholds of the p_T and H_T selection criteria were increased in 2017 and 2018 to sustain data taking in higher pileup conditions.

	2016 (algorithm 1)	2016 (algorithm 2)	2017	2018
$p_{T,1}$ [GeV]	90	45	75	75
$p_{T,2}$ [GeV]	90	45	60	60
$p_{T,3}$ [GeV]	30	45	45	45
$p_{T,4}$ [GeV]	30	45	40	40
H_T [GeV]	-	-	300	330

Table 1: The HLT requirements for the lower bounds on p_T and H_T for the four highest p_T jets in an event are listed for each data-taking year. For data-taking year 2016, events that pass either of two trigger algorithms are used.

The same selection criteria listed in Table 1 are applied to the events after offline reconstruction, and an additional H_T cut of 250 GeV is applied in the 2016 sample. To reduce the number of physics objects that are poorly reconstructed, jets with p_T above 50 GeV are required to pass the tight working point of the PF jet identification algorithm [56], which has an efficiency of 99%. For jets with p_T between 30 and 50 GeV, a separate requirement is applied, specifically that the jet must pass the medium working point of the pileup discriminant [57], which has an efficiency of about 90%. In order to take into account undetected energy carried by a neutrino originating from B hadron decays, the jet p_T is corrected with a multivariate regression technique, as described in [58].

For this analysis, the four jets with the highest DEEPJET b-tagging score are used to identify the X, Y and H candidates. The four jets are required to be the same objects on which the HLT triggered. This selection is performed using ΔR to compare the triggered object and the reconstructed jet. Two datasets are created with different b-tagging score requirements. The main dataset is one that has the potential to contain the signal process and an additional dataset, made predominantly of background events, is used exclusively for modelling the background. The main dataset (4b) is formed by requiring four jets that satisfy the medium working point of the DEEPJET discriminant. The background-dominated dataset (3b) is formed by requiring that three jets satisfy the medium working point and that one jet passes the loose, but fails the medium, working point.

The H and Y candidates are reconstructed by pairing the four jets in the 3b and 4b samples. Out of the possible jet pairs, the one with an invariant mass closest to 125 GeV is selected as the Higgs boson candidate and the remaining pair is the Y candidate, with mass m_{Yreco}. The efficiency of correctly paired candidates is determined, using the simulated samples, by comparing ΔR between the generated Higgs boson and the reconstructed Higgs boson candidate, as well as ΔR between the generated scalar Y and the reconstructed Y candidate. The efficiency ranges from 77.9% to 99.5%, depending on the signal mass hypothesis, where the efficiency is larger for signals with larger differences, $m_{Xreco} - m_{Yreco}$.

For both the 3b and 4b samples, events are subdivided into analysis regions that depend on reconstructed mass of the Higgs boson candidate (m_{Hreco}). The signal region (SR) is defined by $|m_{Hreco} - 125\ \text{GeV}| < 20$ GeV, the validation region (VR) by $20\ \text{GeV} < |m_{Hreco} - 125\ \text{GeV}| <$

30 GeV, and control region (CR) by 30 GeV $< |m_{Hreco} - 125\ \text{GeV}| <$ 60 GeV. The search for signal is performed in the SR of the 4b sample. After the analysis regions are defined, m_{Hreco} is set to be 125 GeV and the momentum is adjusted according to a kinematic fitting procedure.

6 Background modelling

The search for a signal in SR(4b) requires an estimation of the expected background in that region. The background composition in the SR(4b) is dominated by QCD multijet (∼90%) and $t\bar{t}$ (∼10%) events, with the relative contributions determined using the simulated samples discussed in Section 4. A data-driven approach to modelling the background is taken here, using the two-dimensional distribution of 3b events in the $m_{Xreco} - m_{Yreco}$ space as a template.

A BDT-based reweighting method, described in Ref. [59], is used to reweight events in the background-dominated 3b sample to effectively model the difference between the 3b and 4b samples as a function of multiple observables.

The BDT is trained with collision data in the CR(3b) and CR(4b). The obtained weights take into account both residual differences in the event yield normalization and the differences in the shapes of the kinematic distributions between the 4b and 3b samples. The ratio of the event yields of the 3b and 4b samples ranges between 2.21 to 2.68, depending on data-taking year. The differences in the yields for each year depend on both the trigger algorithms and b-tagging efficiencies.

Variables used as input to the BDT are: the p_T of all four selected b-jet candidates, the p_T and η of both the H and the Y candidates, the angular separation ΔR between the two jets that form the reconstructed H candidate (H_{reco}), and ΔR between the two jets that form the reconstructed Y candidate (Y_{reco}). Additionally, the orthogonal distance of the event in the $m_{Xreco} - m_{Yreco}$ plane from the diagonal defined by $m_{Xreco} - m_{Yreco} = 125$ GeV is included as an input variable. This variable is used to provide correlated m_{Xreco} and m_{Yreco} information to the BDT during training.

In order to optimize the training parameters of the BDT model, data in the CR(4b) are compared with the data in CR(3b) after the reweighting is applied. This step makes use of the Kolmogorov-Smirnov distance test (KS) [60], as well as a dedicated BDT discriminator trained to separate the two samples. After optimization, both techniques indicated that the reweighting model performed well. The KS metrics for each reweighted variable decrease, approaching 0, and the areas under the receiver operating characteristic curves of the discriminator are equal to 0.5, indicating the reweighted sample can no longer be distinguished from the target sample.

The BDT reweighting accounts for potential variations in the event yields between the 3b and 4b samples across the analysis regions. To verify this, a statistically independent sample is used to confirm that the application of the technique is able to correctly model the event yields between regions that are dependent on m_{Hreco}.

Validation of the background model is performed by applying the derived weights to the VR(3b) and comparing the kinematic distributions and yields between the reweighted VR(3b) and the VR(4b). It is observed that the kinematic distributions and yields are the same within the considered uncertainties. Comparisons of the m_{Xreco} and m_{Yreco} variables in the validation regions are shown in Fig. 2, for each data-taking year.

An additional test is performed to verify whether a potential signal contamination of the 3b sample induces a bias in the background determination. The test uses the background model

in the signal region (derived by reweighting SR(3b)) data, and simulated signal. Best-fit signal strengths are extracted using the simulated signal and either the background model or a pseudo-data sample constructed using the background model and injected signal contamination. This study is repeated for a subset of the mass hypotheses considered for the search and for injected signal strengths up to 5 times the expected sensitivity of this analysis. In all cases, the results obtained with and without the injected signal contamination are found to be compatible within one standard deviation. These results indicate that this potential self-bias effect of the background model does not impact the final result.

Distributions of the most important analysis observables, $m_{X\text{reco}}$ and $m_{Y\text{reco}}$, for the SR(4b) and reweighted SR(3b) are shown in Fig. 3, including the systematic uncertainties described in Section 7.

7 Systematic uncertainties

Systematic uncertainties are introduced by two components of the analysis: the MC simulated signal and the background estimate, which relies on a data-driven approach. Systematic uncertainties on the signal expectations arise from disagreements between simulations and data, due in part to imperfect modelling of the detector response and the limited number of events in the simulated samples. These correspond to uncertainties that arise from the trigger efficiency, b-tagging efficiency, b-tagging energy regression smearing, jet energy scale, jet energy resolution, pileup reweighting, PDF, parton shower, and luminosity. The largest sources of uncertainty for the signal hypotheses are due to the trigger efficiency and the b-tagging efficiency. The trigger efficiency is the largest contributor to the total uncertainty for signals close to the diagonal in the $m_{X\text{reco}} - m_{Y\text{reco}}$ plane defined by $m_{X\text{reco}} - m_{Y\text{reco}} = 125$ GeV.

The difference between the trigger efficiency in data and simulated events, referred to as a scale factor, is determined by measuring the efficiency in a $t\bar{t}$ dominated data sample and the corresponding MC sample. The uncertainties on the trigger scale factor are implemented as the trigger efficiency systematic uncertainty on the signal events. This component of the uncertainty is higher in the region shortly before the efficiency plateaus to its maximum, leading to the larger impact along the $m_{X\text{reco}} - m_{Y\text{reco}} = 125$ GeV diagonal in the $m_{X\text{reco}} - m_{Y\text{reco}}$ plane. The trigger efficiency contributes up to 35% of the total uncertainty, depending on the signal and data-taking year. The uncertainties on the b-tagging DEEPJET discriminants are accounted for following Ref. [46]. This uncertainty contributes up to 30% of the total uncertainty, with variations based on the signal and the corresponding data-taking year. Jet energy scale and resolution uncertainties are taken into account by varying the jet properties within their uncertainties. A shape uncertainty associated with the b-jet energy regression smearing is determined by shifting the jet resolution up and down by 10% and rerunning the analysis procedures. The uncertainty in the pileup model is determined by varying the inelastic pp cross section by 4.6%. The PDF uncertainties are based on the estimation performed in [22] and range from 1% to 3%, increasing linearly as a function of the $m_{X\text{reco}}$ value of the signal. The parton shower uncertainty of $\sim$7% is derived as in Ref. [61]. The integrated luminosities for the 2016, 2017, and 2018 data-taking years have 1.2–2.5% individual uncertainties [62–64]. The systematics are treated as uncorrelated across the data-taking years, except for the PDF and parton shower uncertainties.

Given the large range over which the search for signal is performed, the contribution of each source of background uncertainty is dependent on which signal mass hypothesis is being considered. The dominant source of background systematic uncertainty is due to the limited number of data events in the SR(3b) region. This source of uncertainty contributes up to 90% of the

total background uncertainty, depending on the signal and data-taking year. The uncertainty on the 4b-to-3b normalization factor is determined by comparing the yields in the 4b-to-3b VRs

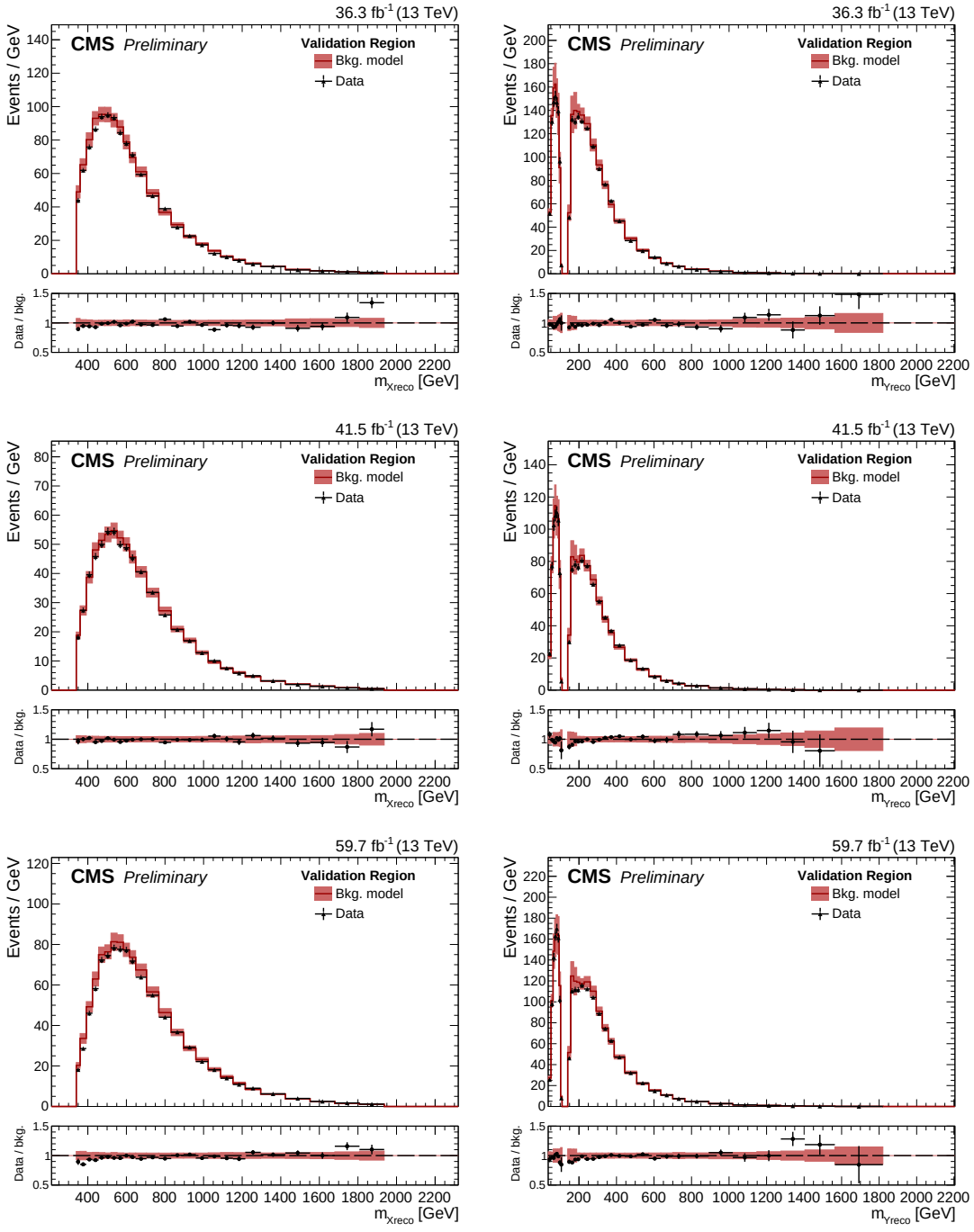

Figure 2: Event distributions in the validation regions for m_{Xreco} (left column) and m_{Yreco} (right column) shown separately for the three data-taking years: 2016, 2017, and 2018 (top, middle, and bottom rows, respectively). The VR(4b) data is in black and BDT reweighted VR(3b) model is in red. For m_{Yreco}, the VR(3b) model uncertainty includes the statistical component added in quadrature with the shape, normalization and non-closure uncertainties. For m_{Xreco}, the VR(3b) uncertainty includes the statistical, shape, and normalization uncertainties. The ratios of VR(3b) over SR(4b) (model over target) are in the lower panels.

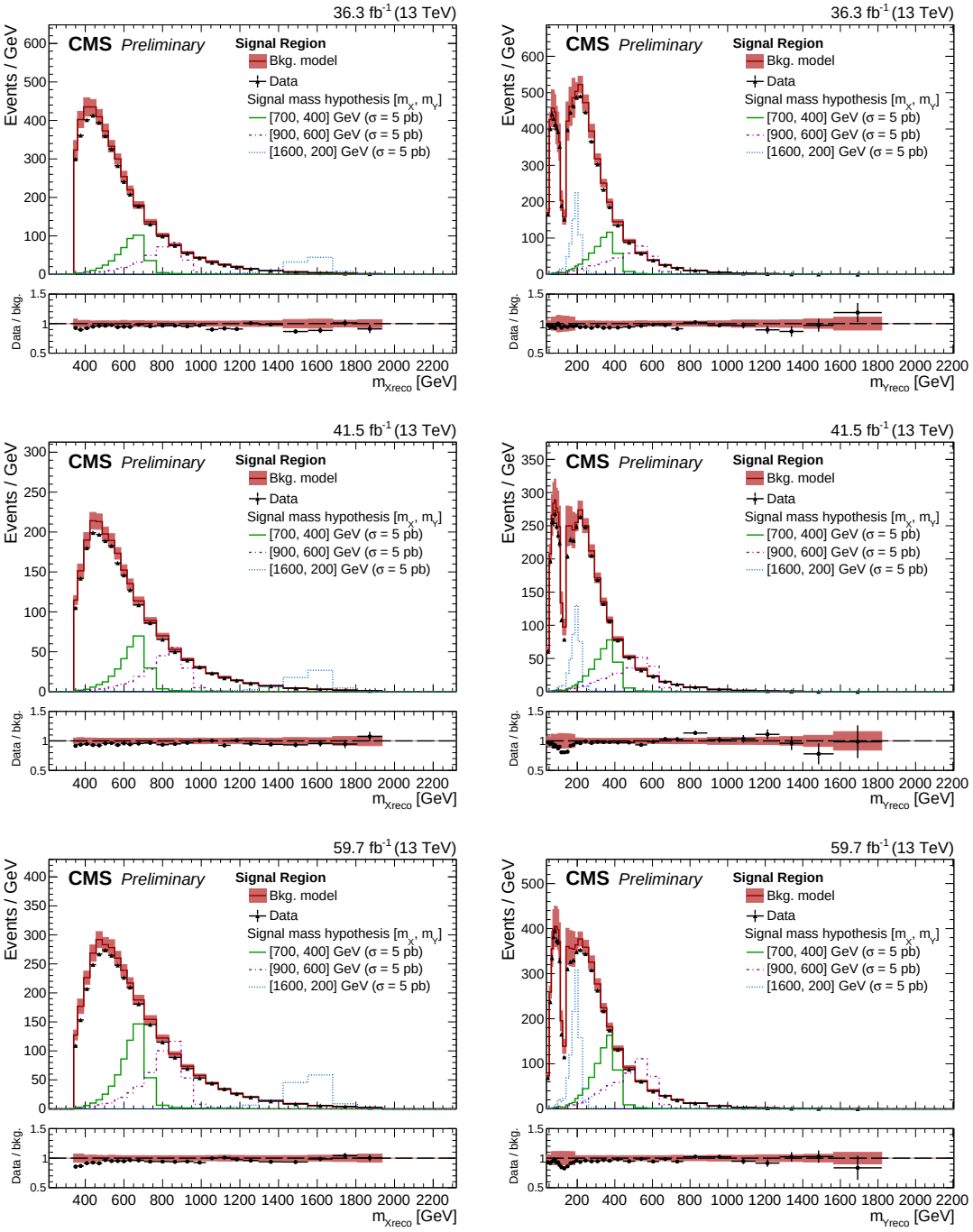

Figure 3: Event distributions in the signal regions for m_{Xreco} (left column) and m_{Yreco} (right column) shown separately for the three data-taking years: 2016, 2017, and 2018 (top, middle, and bottom rows, respectively). The SR(4b) data is in black and BDT reweighted SR(3b) model is in red. For m_{Yreco}, the SR(3b) model uncertainty includes the statistical component added in quadrature with the shape, normalization and non-closure uncertainties. For m_{Xreco}, the SR(3b) uncertainty includes the statistical, shape, and normalization uncertainties. Three selected signal mass hypotheses are overlaid and show the differences in the shape of the distributions of signals and the background. The signal histograms are scaled to have cross section (σ) values of 5 pb. The ratios of SR(3b) over SR(4b) (model over target) are in the lower panels.

and contributes at most 30% of the total uncertainty for any given signal. The potential dependence of the background estimate on the selected boundaries of the CRs is determined by measuring the background in alternative CRs (35 GeV $<$ $|m_{Hreco} - 125\ GeV| < 55$ GeV and 25 GeV $<$ $|m_{Hreco} - 125\ GeV| < 65$ GeV). The derived systematic uncertainty contributes less than 15% of the total uncertainty for all signal hypotheses. Finally, a discrepancy of 10% was observed in the VR(4b) to VR(3b) comparison for m_{Yreco} close to 125 GeV. This is implemented as a systematic uncertainty in the SR for $62 < m_{Yreco} < 188$ GeV.

8 Results

The signal is extracted through a two-dimensional fit in the $m_{Xreco} - m_{Yreco}$ plane. Distributions of events in the SR(4b) for data, background, and one of the signal mass hypotheses are shown for data-taking year 2018 in Fig. 4. In order to minimize the impact of potential mismodelling of the trigger efficiency and jet reconstruction, events for which $m_{Xreco} - m_{Yreco} < 120$ GeV are excluded from the statistical interpretation of results. Regions with high m_{Xreco} and low m_{Yreco} are not considered, since the analysis is not optimized for the decay of highly Lorentz boosted Y resonances. The boundaries in the $m_{Xreco} - m_{Yreco}$ plane that are used for the search range from 340 to 1936 GeV in m_{Xreco}, with a minimum of 36 GeV in m_{Yreco}. For the larger m_{Xreco} values, the m_{Yreco} minimum boundary is increased as: [$m_{Xreco} > 959$, $m_{Yreco} \geq 52$ GeV], [$m_{Xreco} > 1200$, $m_{Yreco} \geq 80$ GeV], [$m_{Xreco} > 1423$, $m_{Yreco} \geq 141$ GeV], [$m_{Xreco} > 1550$, $m_{Yreco} \geq 205$ GeV], and [$m_{Xreco} > 1678$, $m_{Yreco} \geq 770$ GeV].

A binned maximum likelihood fit is performed, using the previously discussed systematic uncertainties as nuisance parameters. The prior distribution used for each nuisance parameter is either Gaussian (for shape uncertainties) or log-normal (for normalization uncertainties). The following results have been determined using the statistical analysis tool COMBINE [65], which is based on the ROOFIT [66] and ROOSTATS [67] frameworks. The observed data and the background are found to be in agreement. The observed data are used to set 95% confidence level (CL) upper limits on the cross section times branching ratio into four b quarks for a new resonance decaying into an H and a Y as a function of the masses of the resonance, X, and the scalar, Y, using the asymptotic modified frequentist method (asymptotic CL_s) [68, 69]. Figure 5 shows the expected and observed 95% CL upper limits as a function of m_X and m_Y. Results are also shown separately for the special case of $X \to HH$ in Fig. 6. The largest excess of the observed over expected cross section times branching ratio is found to have a local (global) significance of 4.1 (2.8) standard deviations for the signal mass hypothesis $m_X = 700$ GeV and $m_Y = 400$ GeV. The global significance is determined with a dedicated "look elsewhere effect" study [70, 71] across the full plane of mass hypotheses used in the initial search. The distribution of observed limits is nearly symmetric and centered around the central expected limits.

In Fig. 7, exclusion limits are compared to the maximum cross section times branching ratio allowed in the NMSSM after experimental constraints from Higgs boson measurements, searches for supersymmetry, flavour physics, and dark matter detection are accounted for. The NMSSM exclusion limits are based on NMSSMTOOLS version 5.6.2 and are obtained from the scans provided in Ref. [72].

Many of these results are the strongest limits produced by CMS for over the broad range of mass hypotheses that were investigated. For mass points with $m_X \leq 1000$ GeV, these results show an average 30% improvement over the expected limits reported using the combination of other channels [18]. For some mass points, the improvements reach to 65 and 75%. The HH results are compatible with previously reported CMS [22] limits. Recent ATLAS results [24] show 50 to 80% stronger limits than the HH results reported here.

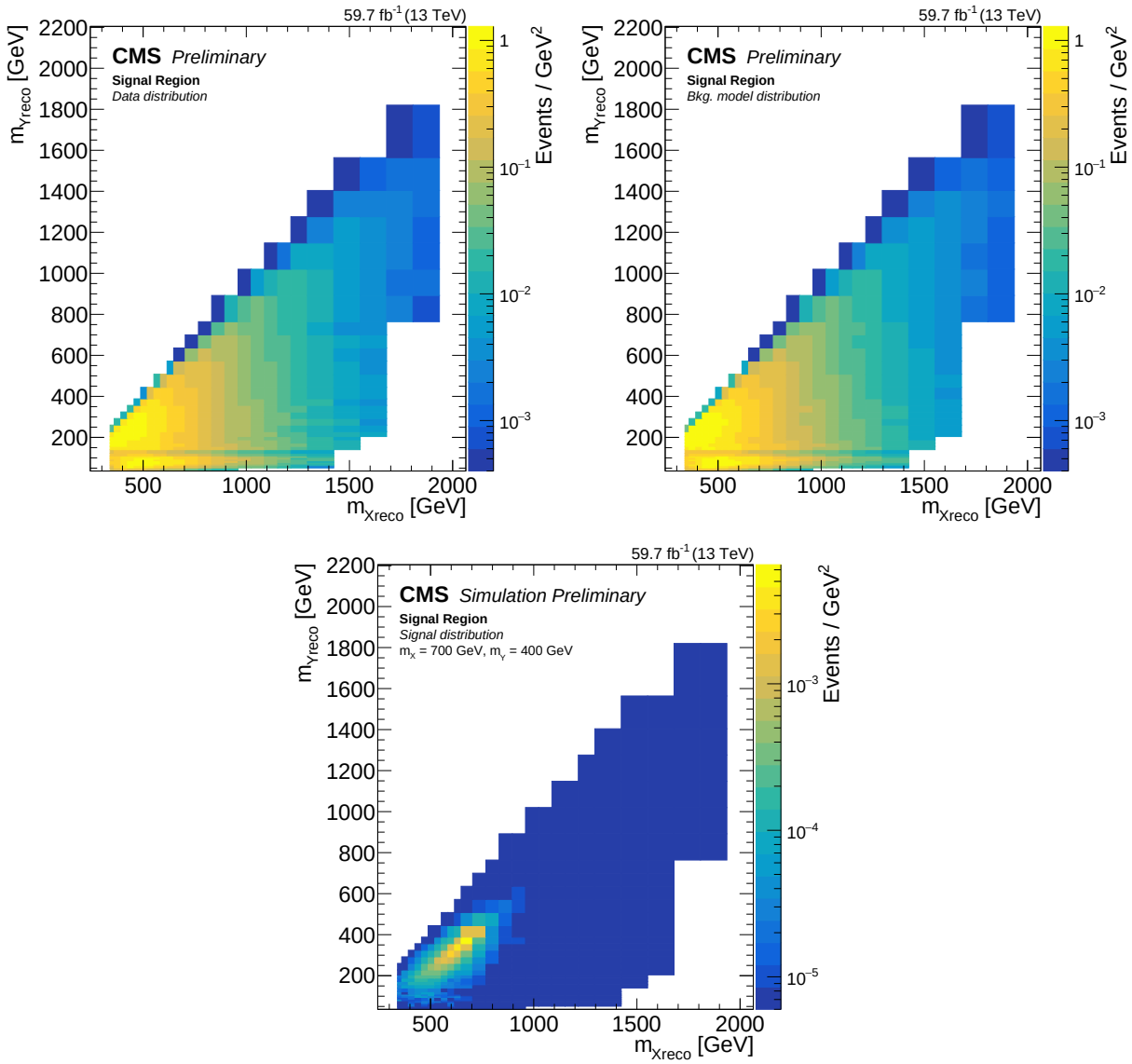

Figure 4: Distributions of the events in the m_{Xreco} – m_{Yreco} plane observed in the SR(4b) in 2018. The top plots show events in data (left) and background model (right). Bottom plot shows distribution of events for the signal hypothesis corresponding to m_X = 700 GeV and m_Y = 400 GeV. In each plot, there are empty bins in the high m_{Xreco} and low m_{Yreco} region. These areas have been excluded because the events are highly boosted.

9 Summary

This note presents a search for a new scalar resonance, X, decaying into a Higgs boson and a new scalar, Y, in the four b-quarks decay channel. The search investigates a range of masses from 400 GeV to 1.6 TeV for the resonance, X, and from 60 GeV up to 1.4 TeV for the scalar, Y. A data sample corresponding to an integrated luminosity of 138 fb^{-1} collected in proton-proton collisions at $\sqrt{s} = 13$ TeV has been used for the search. No evidence for a new signal is observed and upper limits on the signal cross section times branching ratio are set at the 95% confidence level. Results are interpreted in the context of the NMSSM scenario; the results in this note constrain the phase space of this model beyond previous experimental exclusion limits.

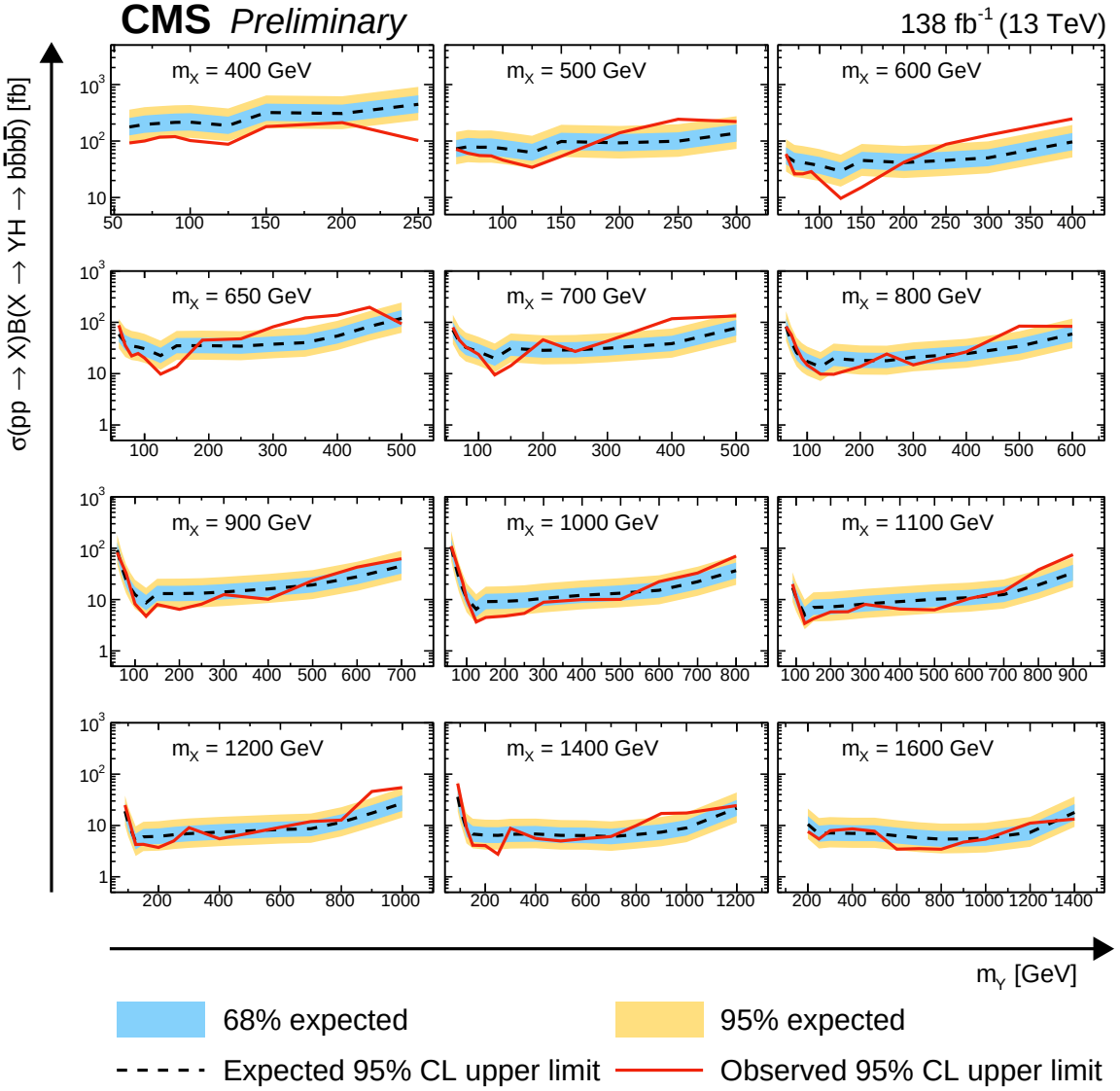

Figure 5: Expected and observed 95% CL upper limits on the production cross section times branching ratio for $X \to YH \to b\bar{b}b\bar{b}$ signal. The limits are shown as a function of m_{Yreco} for selected values of m_{Xreco}. The black dashed and red solid lines represent expected and observed limits, respectively. The blue and yellow bands represent the ± 1 and ± 2 standard deviations for the expected limit, respectively. The largest excess of the observed limit over the expected limit is for m_{Xreco} = 700 GeV and m_{Yreco} = 400 GeV.

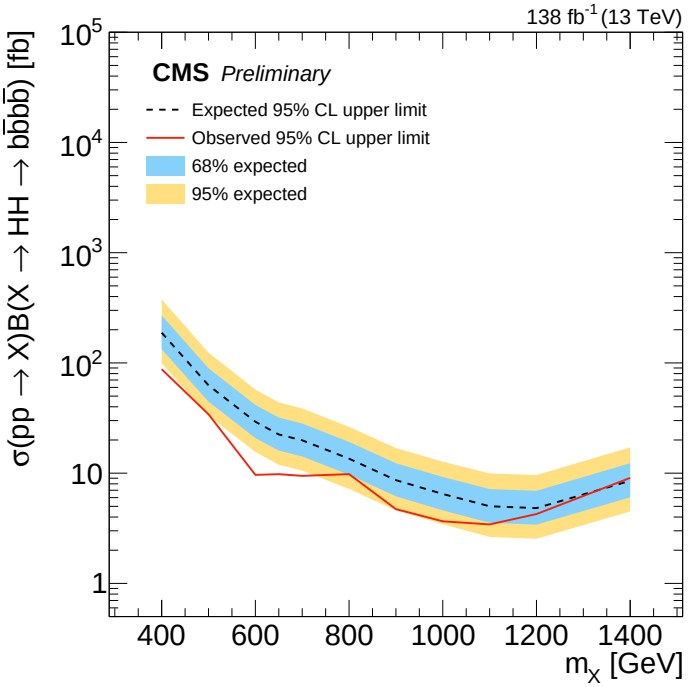

Figure 6: Expected and observed 95% CL upper limits on the production cross section times branching ratio for $X \to HH \to b\bar{b}b\bar{b}$ signal. The black dashed and red solid lines represent expected and observed limits, respectively. The blue and yellow bands represent the ± 1 and ± 2 standard deviations for the expected limit, respectively.

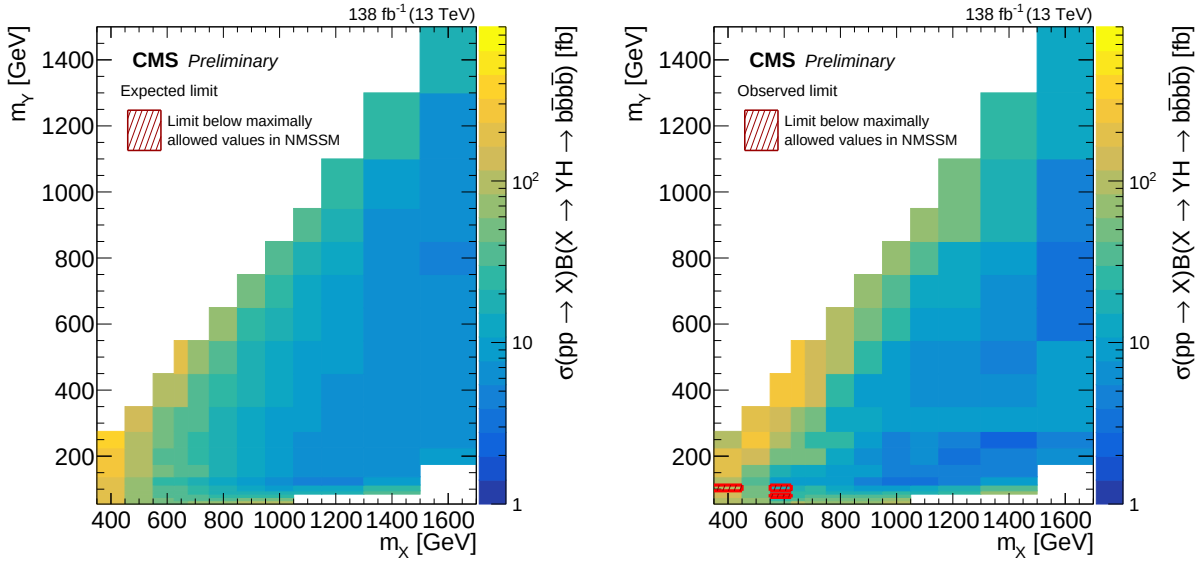

Figure 7: Expected and observed 95% CL upper limits on production cross section times branching ratio for $X \to YH \to b\bar{b}b\bar{b}$ signals shown in the two-dimensional m_X and m_Y plane. These limits are compared to the maximally allowed cross section times branching ratio values determined with NMSSM and taking into account previous experimental constraints. The NMSSM limits are obtained with NMSSMTOOLS 5.6.2 and appear in Ref. [72]. A few mass hypotheses where the observed limits are more restrictive than the NMSSM limits are indicated by the red hatched areas.

Acknowledgments

References

[1] ATLAS Collaboration, "Observation of a new particle in the search for the Standard Model Higgs boson with the ATLAS detector at the LHC", *Phys. Lett. B* **716** (2012) 1, doi:10.1016/j.physletb.2012.08.020, arXiv:1207.7214.

[2] CMS Collaboration, "Observation of a new boson at a mass of 125 GeV with the CMS experiment at the LHC", *Phys. Lett. B* **716** (2012) 30, doi:10.1016/j.physletb.2012.08.021, arXiv:1207.7235.

[3] CMS Collaboration, "Observation of a new boson with mass near 125 GeV in pp collisions at $\sqrt{s}$ = 7 and 8 TeV", *JHEP* **06** (2013) 081, doi:10.1007/JHEP06(2013)081, arXiv:1303.4571.

[4] U. Ellwanger, C. Hugonie, and A. M. Teixeira, "The Next-to-Minimal Supersymmetric Standard Model", *Phys. Rep.* **496** (2010) 1, doi:10.1016/j.physrep.2010.07.001, arXiv:0910.1785.

[5] M. Maniatis, "The Next-to-Minimal Supersymmetric extension of the Standard Model reviewed", *Int. J. Mod. Phys. A* **25** (2010) 3505, doi:10.1142/S0217751X10049827, arXiv:0906.0777.

[6] T. Robens, T. Stefaniak, and J. Wittbrodt, "Two-real-scalar-singlet extension of the SM: LHC phenomenology and benchmark scenarios", *Eur. Phys. J. C* **80** (2020), no. 2, 151, doi:10.1140/epjc/s10052-020-7655-x, arXiv:1908.08554.

[7] A. Carvalho, "Gravity particles from Warped Extra Dimensions, predictions for LHC", 3, 2014. arXiv:1404.0102.

[8] U. Ellwanger and M. Rodriguez-Vazquez, "Simultaneous search for extra light and heavy Higgs bosons via cascade decays", *JHEP* **11** (2017) 008, doi:10.1007/JHEP11(2017)008, arXiv:1707.08522.

[9] Z. Kang et al., "Probing the CP-even Higgs sector via $H_3 \to H_2 H_1$ in the natural next-to-minimal supersymmetric standard model", *Phys. Rev. D* **88** (2013), no. 1, 015006, doi:10.1103/PhysRevD.88.015006, arXiv:1301.0453.

[10] S. F. King, M. Mühlleitner, R. Nevzorov, and K. Walz, "Discovery Prospects for NMSSM Higgs Bosons at the High-Energy Large Hadron Collider", *Phys. Rev. D* **90** (2014), no. 9, 095014, doi:10.1103/PhysRevD.90.095014, arXiv:1408.1120.

[11] M. Carena et al., "Alignment limit of the NMSSM Higgs sector", *Phys. Rev. D* **93** (2016), no. 3, 035013, doi:10.1103/PhysRevD.93.035013, arXiv:1510.09137.

[12] U. Ellwanger and M. Rodriguez-Vazquez, "Discovery Prospects of a Light Scalar in the NMSSM", *JHEP* **02** (2016) 096, doi:10.1007/JHEP02(2016)096, arXiv:1512.04281.

[13] R. Costa, M. Mühlleitner, M. O. P. Sampaio, and R. Santos, "Singlet Extensions of the Standard Model at LHC Run 2: Benchmarks and Comparison with the NMSSM", *JHEP* **06** (2016) 034, doi:10.1007/JHEP06(2016)034, arXiv:1512.05355.

[14] ATLAS Collaboration, "Search for a resonance decaying into a scalar particle and a Higgs boson in the final state with two bottom quarks and two photons in proton-proton collisions at a center of mass energy of 13 TeV with the ATLAS detector", 4, 2024. arXiv:2404.12915. Submitted to JHEP.

[15] CMS Collaboration, "Search for a new resonance decaying into two spin-0 bosons in a final state with two photons and two bottom quarks in proton-proton collisions at $\sqrt{s}$ = 13 TeV", *JHEP* **05** (2024) 316, doi:10.1007/JHEP05(2024)316, arXiv:2310.01643.

[16] CMS Collaboration, "Search for a heavy Higgs boson decaying into two lighter Higgs bosons in the $\tau\tau$bb final state at 13 TeV", *JHEP* **11** (2021) 057, doi:10.1007/JHEP11(2021)057, arXiv:2106.10361.

[17] CMS Collaboration, "Search for a massive scalar resonance decaying to a light scalar and a Higgs boson in the four b quarks final state with boosted topology", *Phys. Lett. B* **842** (2023) 137392, doi:10.1016/j.physletb.2022.137392, arXiv:2204.12413.

[18] CMS Collaboration, "Searches for Higgs Boson Production through Decays of Heavy Resonances", 3, 2024. arXiv:2403.16926. Submitted to Phys. Rep.

[19] C. Csáki, J. Hubisz, and S. J. Lee, "Radion phenomenology in realistic warped space models", *Phys. Rev. D* **76** (2007) 125015, doi:10.1103/PhysRevD.76.125015, arXiv:0705.3844.

[20] M. Gouzevitch et al., "Scale-invariant resonance tagging in multijet events and new physics in Higgs pair production", *JHEP* **07** (2013) 148, doi:10.1007/JHEP07(2013)148, arXiv:1303.6636.

[21] R. Barbieri et al., "Exploring the Higgs sector of a most natural NMSSM", *Phys. Rev. D* **87** (2013), no. 11, 115018, doi:10.1103/PhysRevD.87.115018, arXiv:1304.3670.

[22] CMS Collaboration, "Search for resonant pair production of Higgs bosons decaying to bottom quark-antiquark pairs in proton-proton collisions at 13 TeV", *JHEP* **08** (2018) 152, doi:10.1007/JHEP08(2018)152, arXiv:1806.03548.

[23] ATLAS Collaboration, "Search for pair production of Higgs bosons in the $b\bar{b}b\bar{b}$ final state using proton-proton collisions at $\sqrt{s} = 13$ TeV with the ATLAS detector", *JHEP* **01** (2019) 30, doi:10.1007/JHEP01(2019)030, arXiv:1804.06174.

[24] ATLAS Collaboration, "Search for resonant pair production of Higgs bosons in the $b\bar{b}b\bar{b}$ final state using pp collisions at $\sqrt{s}$ = 13 TeV with the ATLAS detector", *Phys. Rev. D* **105** (2022), no. 9, 092002, doi:10.1103/PhysRevD.105.092002, arXiv:2202.07288.

[25] CMS Collaboration, "Search for Higgs boson pair production in events with two bottom quarks and two tau leptons in proton-proton collisions at $\sqrt{s}$ =13 TeV", *Phys. Lett. B* **778** (2018) 101, doi:10.1016/j.physletb.2018.01.001, arXiv:1707.02909.

[26] ATLAS Collaboration, "Combination of searches for heavy resonances decaying into bosonic and leptonic final states using 36 fb^{-1} of proton-proton collision data at $\sqrt{s} = 13$ TeV with the ATLAS detector", *Phys. Rev. D* **98** (2018) 052008, doi:10.1103/PhysRevD.98.052008, arXiv:1808.02380.

[27] CMS Collaboration, "Search for Higgs boson pair production in the $\gamma\gamma b\bar{b}$ final state in pp collisions at $\sqrt{s} = 13$ TeV", *Phys. Lett. B* **788** (2019) 7, doi:10.1016/j.physletb.2018.10.056, arXiv:1806.00408.

[28] CMS Collaboration, "Search for resonant and nonresonant Higgs boson pair production in the $b\bar{b}\ell\nu\ell\nu$ final state in proton-proton collisions at $\sqrt{s} = 13$ TeV", *JHEP* **01** (2018) 54, doi:10.1007/JHEP01(2018)054, arXiv:1708.04188.

[29] CMS Collaboration, "Search for resonant pair production of Higgs bosons in the *bbZZ* channel in proton-proton collisions at $\sqrt{s} = 13$ TeV", *Phys. Rev. D* **102** (2020), no. 3, 032003, doi:10.1103/PhysRevD.102.032003, arXiv:2006.06391.

[30] CMS Collaboration, "Search for Higgs boson pairs decaying to WW*WW*, WW*$\tau\tau$, and $\tau\tau\tau\tau$ in proton-proton collisions at $\sqrt{s}$ = 13 TeV", *JHEP* **07** (2023) 095, doi:10.1007/JHEP07(2023)095, arXiv:2206.10268.

[31] ATLAS Collaboration, "Combination of Searches for Resonant Higgs Boson Pair Production Using pp Collisions at $\sqrt{s}$ = 13 TeV with the ATLAS Detector", *Phys. Rev. Lett.* **132** (2024), no. 23, 231801, doi:10.1103/PhysRevLett.132.231801, arXiv:2311.15956.

[32] ATLAS Collaboration, "Combination of searches for Higgs boson pair production in *pp* collisions at $\sqrt{s}$ = 13 TeV with the ATLAS detector.", 5, 2024. ATLAS-CONF-2024-006.

[33] CMS Collaboration, "The CMS experiment at the CERN LHC", *JINST* **3** (2008) S08004, doi:10.1088/1748-0221/3/08/S08004.

[34] CMS Collaboration, "Development of the CMS detector for the CERN LHC Run 3", *JINST* **19** (2024), no. 05, P05064, doi:10.1088/1748-0221/19/05/P05064, arXiv:2309.05466.

[35] CMS Collaboration, "Performance of the CMS Level-1 trigger in proton-proton collisions at $\sqrt{s} = 13$ TeV", *JINST* **15** (2020) P10017, doi:10.1088/1748-0221/15/10/P10017, arXiv:2006.10165.

[36] CMS Collaboration, "The CMS trigger system", *JINST* **12** (2017) P01020, doi:10.1088/1748-0221/12/01/P01020, arXiv:1609.02366.

[37] CMS Collaboration, "Electron and photon reconstruction and identification with the CMS experiment at the CERN LHC", *JINST* **16** (2021) P05014, doi:10.1088/1748-0221/16/05/P05014, arXiv:2012.06888.

[38] CMS Collaboration, "Performance of the CMS muon detector and muon reconstruction with proton-proton collisions at $\sqrt{s} = 13$ TeV", *JINST* **13** (2018) P06015, doi:10.1088/1748-0221/13/06/P06015, arXiv:1804.04528.

[39] CMS Collaboration, "Description and performance of track and primary-vertex reconstruction with the CMS tracker", *JINST* **9** (2014) P10009, doi:10.1088/1748-0221/9/10/P10009, arXiv:1405.6569.

[40] CMS Collaboration, "Particle-flow reconstruction and global event description with the CMS detector", *JINST* **12** (2017) P10003, doi:10.1088/1748-0221/12/10/P10003, arXiv:1706.04965.

[41] CMS Collaboration, "Performance of reconstruction and identification of τ leptons decaying to hadrons and ν_τ in pp collisions at $\sqrt{s} = 13$ TeV", *JINST* **13** (2018) P10005, doi:10.1088/1748-0221/13/10/P10005, arXiv:1809.02816.

[42] CMS Collaboration, "Jet energy scale and resolution in the CMS experiment in pp collisions at 8 TeV", *JINST* **12** (2017) P02014, doi:10.1088/1748-0221/12/02/P02014, arXiv:1607.03663.

[43] CMS Collaboration, "Performance of missing transverse momentum reconstruction in proton-proton collisions at $\sqrt{s} = 13$ TeV using the CMS detector", *JINST* **14** (2019) P07004, doi:10.1088/1748-0221/14/07/P07004, arXiv:1903.06078.

[44] M. Cacciari, G. P. Salam, and G. Soyez, "The anti-k_T jet clustering algorithm", *JHEP* **04** (2008) 063, doi:10.1088/1126-6708/2008/04/063, arXiv:0802.1189.

[45] M. Cacciari, G. P. Salam, and G. Soyez, "FastJet user manual", *Eur. Phys. J. C* **72** (2012) 1896, doi:10.1140/epjc/s10052-012-1896-2, arXiv:1111.6097.

[46] E. Bols et al., "Jet Flavour Classification Using DeepJet", *JINST* **15** (2020), no. 12, P12012, doi:10.1088/1748-0221/15/12/P12012, arXiv:2008.10519.

[47] CMS Collaboration, "Identification of heavy-flavour jets with the CMS detector in pp collisions at 13 TeV", *JINST* **13** (2018) P05011, doi:10.1088/1748-0221/13/05/P05011, arXiv:1712.07158.

[48] J. Alwall et al., "The automated computation of tree-level and next-to-leading order differential cross sections, and their matching to parton shower simulations", *JHEP* **07** (2014) 079, doi:10.1007/JHEP07(2014)079, arXiv:1405.0301.

[49] NNPDF Collaboration, "Parton distributions for the LHC Run II", *JHEP* **04** (2015) 040, doi:10.1007/JHEP04(2015)040, arXiv:1410.8849.

[50] S. Alioli, P. Nason, C. Oleari, and E. Re, "NLO vector-boson production matched with shower in POWHEG", *JHEP* **07** (2008) 060, doi:10.1088/1126-6708/2008/07/060, arXiv:0805.4802.

[51] P. Nason, "A New method for combining NLO QCD with shower Monte Carlo algorithms", *JHEP* **11** (2004) 040, doi:10.1088/1126-6708/2004/11/040, arXiv:hep-ph/0409146.

[52] M. Czakon and A. Mitov, "Top++: A Program for the Calculation of the Top-Pair Cross-Section at Hadron Colliders", *Comput. Phys. Commun.* **185** (2014) 2930, doi:10.1016/j.cpc.2014.06.021, arXiv:1112.5675.

[53] J. M. Campbell, R. K. Ellis, and C. Williams, "Vector boson pair production at the LHC", *JHEP* **07** (2011) 018, doi:10.1007/JHEP07(2011)018, arXiv:1105.0020.

[54] T. Sjöstrand et al., "An introduction to PYTHIA 8.2", *Comput. Phys. Commun.* **191** (2015) 159, doi:10.1016/j.cpc.2015.01.024, arXiv:1410.3012.

[55] GEANT4 Collaboration, "GEANT4–a simulation toolkit", *Nucl. Instrum. Meth. A* **506** (2003) 250, doi:10.1016/S0168-9002(03)01368-8.

[56] CMS Collaboration, "Jet algorithms performance in 13 TeV data", Technical Report CMS-PAS-JME-16-003, CERN, Geneva, 2017.

[57] CMS Collaboration, "Pileup mitigation at CMS in 13 TeV data", *JINST* **15** (2020) P09018, doi:10.1088/1748-0221/15/09/p09018, arXiv:2003.00503.

[58] CMS Collaboration, "A Deep Neural Network for Simultaneous Estimation of b Jet Energy and Resolution", *Comput. Softw. Big Sci.* **4** (2020), no. 1, 10, doi:10.1007/s41781-020-00041-z, arXiv:1912.06046.

[59] A. Rogozhnikov, "Reweighting with Boosted Decision Trees", *J. Phys. Conf. Ser.* **762** (2016), no. 1, 012036, doi:10.1088/1742-6596/762/1/012036, arXiv:1608.05806.

[60] Chakravarti, Laha, and Roy, "Handbook of Methods of Applied Statistics, Volume I". John Wiley and Sons, 1967.

[61] CMS Collaboration, "Search for Higgs Boson Pair Production in the Four b Quark Final State in Proton-Proton Collisions at $\sqrt{s} = 13$ TeV ", *Phys. Rev. Lett.* **129** (2022), no. 8, 081802, doi:10.1103/PhysRevLett.129.081802, arXiv:2202.09617.

[62] CMS Collaboration, "Precision luminosity measurement in proton-proton collisions at $\sqrt{s} = 13$ TeV in 2015 and 2016 at CMS", *Eur. Phys. J. C* **81** (2021) 800, doi:10.1140/epjc/s10052-021-09538-2, arXiv:2104.01927.

[63] CMS Collaboration, "CMS luminosity measurement for the 2017 data-taking period at $\sqrt{s} = 13$ TeV", CMS Physics Analysis Summary CMS-PAS-LUM-17-004, 2018.

[64] CMS Collaboration, "CMS luminosity measurement for the 2018 data-taking period at $\sqrt{s} = 13$ TeV", CMS Physics Analysis Summary CMS-PAS-LUM-18-002, 2019.

[65] CMS Collaboration, "The CMS statistical analysis and combination tool: COMBINE", 2024. arXiv:2404.06614. Submitted to *Comput. Softw. Big Sci.*

[66] W. Verkerke and D. P. Kirkby, "The RooFit toolkit for data modeling", *eConf* **C0303241** (2003) MOLT007, arXiv:physics/0306116.

[67] L. Moneta et al., "The RooStats Project", *PoS* **ACAT2010** (2010) 057, doi:10.22323/1.093.0057, arXiv:1009.1003.

[68] T. Junk, "Confidence level computation for combining searches with small statistics", *Nucl. Instrum. Meth. A* **434** (1999) 435, doi:10.1016/S0168-9002(99)00498-2, arXiv:hep-ex/9902006.

[69] A. L. Read, "Presentation of search results: the CL_s technique", *J. Phys. G* **28** (2002) 2693, doi:10.1088/0954-3899/28/10/313.

[70] E. Gross and O. Vitells, "Trial factors for the look elsewhere effect in high energy physics", *Eur. Phys. J. C* **70** (2010) 525, doi:10.1140/epjc/s10052-010-1470-8, arXiv:1005.1891.

[71] O. Vitells and E. Gross, "Estimating the significance of a signal in a multi-dimensional search", *Astroparticle Physics* **35** (2011), no. 5, 230, doi:10.1016/j.astropartphys.2011.08.005, arXiv:1105.4355.

[72] U. Ellwanger and C. Hugonie, "Benchmark planes for Higgs-to-Higgs decays in the NMSSM", *Eur. Phys. J. C* **82** (2022), no. 5, 406, doi:10.1140/epjc/s10052-022-10364-3, arXiv:2203.05049.